Programmable graphene-based microfluidic sensor for DNA detection

Agnes Purwidyantri[1,*], Andrey Ipatov[1], Telma Domingues[1,2], Jérôme Borme[1], Marco Martins[1], Pedro Alpuim[1,2,*], Marta Prado[1]

[1]International Iberian Nanotechnology Laboratory (INL), Av. Mestre José Veiga, 4715-330 Braga, Portugal

[2]Center of Physics, University of Minho, 4710-057 Braga, Portugal

*) Corresponding author(s)

agnes.purwidyantri@inl.int

pedro.alpuim.us@inl.int

Abstract

This study presents the development of a lab-on-a-chip (LoC) by integrating a graphene field-effect transistor (FET) chip with a programmable microfluidic device for DNA detection. The real-time biochemical events on the graphene FET chip were monitored through Dirac voltage shift data from the portable graphene curve reader with changes dependent on the fluidic flow into the sensing interface by a fully automated programmable microfluidic system. High sensitivity with high reliability can be obtained with a nine-graphene sensor layout on a single chip. The portable graphene curve reader also provides a tunable electrical parameter setup and straightforward data acquisition. Fluidic control was performed through a multi-position valve, allowing sequential commands for liquid injection into the polydimethylsiloxane (PDMS) flow cell mounted on the sensing chip. The flow cell design with impinging jet geometry and the microfluidic system packaging offer high precision and portability as a less laborious and low-cost sensing setup. The merged system allows for various functionalities, including probe DNA (pDNA) immobilization, a blocking step, and DNA hybridization with stable signal output autonomously, even in a long-run experimental setup. As a DNA sensor, the proposed prototype has demonstrated a high sensitivity of ~44 mV/decade of target DNA concentration, with an outstanding limit of detection (LoD) of ~0.642 aM, making it one of the most sensitive sensors reported up to date. The programmable device has demonstrated essential versatilities for biomolecular detection in a fully portable and automated platform.

Keywords: lab-on-a-chip (LoC), graphene field-effect transistor (FET), programmable microfluidic, DNA sensor.

1. Introduction

Micro total analysis systems (μTAS) and lab-on-a-chip (LoC) have emerged in recent decades and are evolving rapidly, particularly regarding their use in decentralized settings. The advancement of fluidic processing in microchannel architectures of extremely low volume is of great interest for vast applications [1], such as biomedical screening requiring fast diagnostics, like in a pandemic scenario. This advancement has reinforced the revenues of microfluidic-based point-of-care devices with a durable impact on various industries [2], [3]. Besides, these systems also play an active role in high throughput, contactless and fast detection in different points of the food supply chain [4], [5]. The significant advantages of microfluidic systems rely on miniaturization to integrate controllable liquid flow, lower consumption of reagents and samples, and faster analysis, turning complex analyses into more cost-effective, fast, less hazardous for both the operator and the environment, and less laborious protocols with lower energy consumption. Precise flow control systems combining a micro-pump and highly encapsulated flow cell for the micro reaction chamber is an essential parameter in building up an automated microfluidic system that can provide pumping, solution distribution, mixing, liquid manipulation, surface functionalization, washing, and many other fluidic manipulation tasks throughout the whole detection operation [6]. Designing a pump control and valving system is a robust microfluidic platform development strategy [7]–[9]. Programming microfluidics to execute biological protocols can be a game-changer for real-time, extensive, autonomous experiments.

Among other outstanding nanomaterials, graphene has been preferred for fabricating LoC devices due to its excellent characteristics. Single-layer graphene is noted for its transparency, 98% transparent to visible light with only one atom of thickness. The ultrathin (~0.35 nm) and ultra-light honeycomb structure of graphene owing to its planar density of 0.77 mg/m^2 have resulted in outstanding chemical and physical properties for futuristic, ground-breaking technology with many possibilities for different applications [10]–[12]. Graphene also exhibits unique mechanical properties with a Young's modulus of 1.0 TPa and intrinsic strength of 130 GPa, extremely high thermal conductivity with a value up to 8000 W/m.K, and excellent electron mobility of up to $2x10^5$ $cm^2V^{-1}s^{-1}$, which render graphene as the most conductive material at room temperature, with a conductivity of 1.42 $x10^6$ S/m and a sheet resistance of 125 Ω/sq [13], [14]. Graphene can be easily functionalized, making it a good candidate for biosensor materials [15]–[18]. The integration of graphene with microfluidics substantially improves analytical detection for more practical applications. A nanoengineered mesoporous L-cysteine-graphene (Cys-RGO) hydrogel has been reported to show dual-modality sensing on a microfluidic surface plasmon resonance (SPR) chip to detect human cardiac myoglobin molecules [19]. A microfluidic device incorporating single-layer graphene from a mechanical exfoliation process has also been shown to effectively detect chlorpyrifos, a type of pesticide, in the femtomolar concentration range [20]. The engineering of graphene oxide nanosheets embedded in a microfluidic system has been reported to promote highly sensitive natural killer (NK) cell isolation and on-chip short-term culture for NK-exo biogenesis for cancer diagnosis [21].

Graphene field-effect transistors (graphene FETs) have gained tremendous attention due to their distinguished properties for biosensor development, particularly for DNA detection [22]–[24]. Graphene FETs are noted to be extremely sensitive to gate potential changes in a liquid environment. The critical issues in integrating a graphene FET chip with a microfluidic system are performing stable probe DNA (pDNA) immobilization onto the graphene surface and maintaining graphene conductivity for highly sensitive detection in a confined dynamic flow setup. Several graphene functionalization strategies have been reported. However, their

suitability for integration in the LoC system requires meticulous analysis. For instance, conventional silane-based surface engineering disrupts the graphene aromatic structure, decreasing electron mobility, rendering it unsuitable for a graphene-FET system [25]. Another simple scheme employs direct immobilization of pDNA by π-π stacking, followed by the hybridization of target DNA (tDNA) with a fully matching sequence that will detach the double-stranded (dsDNA) from the graphene surface. The detachment of the pDNA from graphene by negative charge repulsion between the phosphate backbone of the newly formed dsDNA and the graphene surface is not applicable for the flowthrough chip configuration [26], [27]. One effective immobilization technique for graphene is by pDNA attachment via a pyrene butyric acid linker. The pyrene end of the linker is firmly attached to the graphene basal plane through π-π stacking, while the carboxylated end of the linker provides a covalent bond with the amine-tagged pDNA [28]–[30]. This pyrene butyric-based functionalization maintains graphene's high conductivity without damaging the graphene crystal lattice and ensures probe stability in a dynamic flow environment.

The present study introduces a prototype LoC integrating a graphene FET chip with a programmable microfluidics system enabling on-demand sampling via multi-sample injection, compartmentalization, and manipulation of multiple aqueous volumes. The self-developed software for control and data collection of graphene FET transfer curve acquisition and the microfluidic system can be operated simultaneously to obtain transient real-time detection. We demonstrate the utility of the integrated system for sensitive, rapid, portable, and highly automated DNA hybridization screening. The device also shortens the time for effective pDNA surface immobilization, dispensing with the overnight incubation typically performed in the conventional static-drop probe modification on graphene. In addition, we also present the effectivity of the forward-reverse mixing technique in the pDNA kinetic activity and the DNA hybridization stage. The proposed system demonstrates high sensitivity and a considerably low limit of detection (LoD) and specificity of detection regarding complementary and non-complementary DNA targets. Therefore, it opens up possibilities for broader application, such as direct and on-site varietal discrimination in plants and food, pollutant screening, environmental control, and early clinical diagnostics.

2. Materials and Methods

2.1. Materials

A highly purified copper foil (>99.99%) for growing graphene was purchased from Alfa Aesar (Ward Hill, MA, USA) or from Goodfellow GmbH (Hamburg, Germany). Phosphate buffered saline (PBS), NaCl and $MgCl_2$ for DNA hybridization buffer mixture, 1-Dodecanethiol (DDT) as gold passivation layer, ethanolamine (ETA) blocking agent, and 1-pyrene butyric acid succinimidyl ester (PBSE) for graphene surface linker to anchor the probe DNA and other solvents, such as acetone, ethyl acetate, were purchased from Sigma-Aldrich. A MilliQ system provided the deionized water with resistivity at 25°C = 18.2 M. For the DNA hybridization study, specific sequences of synthetic oligonucleotides were derived from the flavanone-3-hydroxylase (F3H) gene of some Portuguese grape varieties, verified using Geneious Prime 2020 software (https://www.geneious.com). For this particular study, a specific sequence from the F3H gene of the Tinta Amarela variety was used. The probe DNA (pDNA), complementary target DNA (comp-tDNA), and non-complementary target DNA (non-comp-tDNA) were synthesized by Metabion International AG (Planegg, Germany), with the detailed sequences listed in Table 1.

Table 1. The DNA sequences used in this study.

DNA Name	Sequence
Probe DNA (pDNA)	5´-C6-amine-GCGAAAGGCTGAAGCTAATCTTTTCTTTGTCTTTG-3
Complementary target (comp-tDNA)	5´-CAAAGACAAAGAAAAGATTAGCTTCAGCCTTTC GC-3´
Non-complementary target DNA (non-comp-tDNA)	5´-GGACCTTTCGTGGTGAATCTTGGAGACCATGGACA-3´

2.2 Methods

2.2.1 Device Fabrication

The automated microfluidic system consists of a syringe pump and a ten-port multi-position valve (FIAlab Instruments, Inc, WA, USA). The valve and the pump were placed in a single PMMA box with a wall thickness of 4 mm. PMMA plates (Plexicril Company, Braga, Portugal) for the box were cut with a laser cutter machine (Widlaser LS1390Plus, Portugal). Finally, all the electronic components (Digi-Key Electronics, MN, USA) and the valving modules were designed and configured in a polymethylmethacrylate (PMMA) box with dimensions of ~15×25×21 cm^3 (length×width×height). The integrated setup, including the portable graphene sensor and the microfluidic system, is illustrated in Figure 1a. The automated flow-injection system and the software construction are explained in detail in Supplementary Materials (Figure S1). The photograph of the ready-to-use graphene FET chip with the PDMS flow cell mounted with the PMMA clasps for liquid confinement can be seen in Figure 1b. The detailed procedure of the flow cell fabrication is presented in the Supplementary Materials (Figure S2). The fabrication of the graphene FET chip was reported in our previous work [23]. In brief, the chip was produced on an 8-inch Si wafer (B-doped, 8-30 Ω) covered with 200 nm SiO_2. A 5nm Cr layer was employed as an adhesion layer for the deposition of 40 nm gold. A photolithography procedure was performed to pattern the source (S), drain (D), and gate (G). The passivation of current lines was completed with reactive ion etching (RIE) patterning of a 250 nm multilayer SiO_2 and Si_3N_x stack. After the chip fabrication, the graphene film was transferred onto the chips uniformly [31]. The uniformity of graphene after the transfer process was observed using a Nikon Eclipse L200N optical microscope for graphene on a silicon substrate.

The process was continued with wafer dicing, in which a chip is constituted of nine graphene sensors with a receded gate. The chip layout is depicted in Figure 1c. The graphene channel's dimension is 25×75 μm^2 (Figure 1d), and the actual gate area exposed to the solution is ≈ 1.51×10^6 μm^2. The chip was then wire-bonded and packed in PCB for measurement with the portable system. The graphene quality was measured using a confocal Raman spectroscope equipped with a WITec Alpha300 R confocal instrument using a set of Zeiss microscope lenses. Raman spectra were acquired at room temperature utilizing 532 nm and 633 nm laser excitation in a backscattering geometry at a power output of 1.5 mW, 50× lens objective, numerical aperture of 0.7, and a 600 groove/mm grating for three acquisitions in a 10s acquisition time to collect Raman spectra at different positions on the graphene channel. The quality of the graphene was screened by Raman mapping.

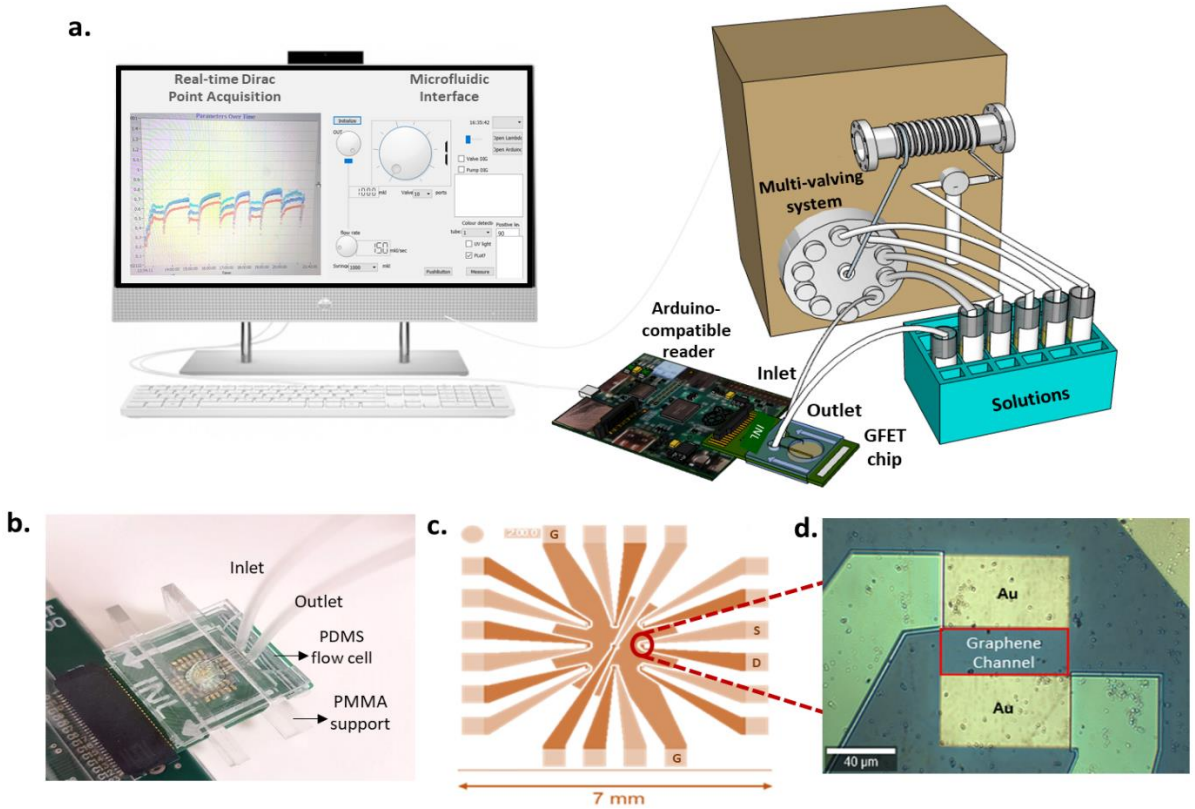

Figure 1. a. The integrated graphene FET chip and programmable microfluidic system with the built-in software for DNA detection, b. The photograph of graphene FET chip mounted with PDMS flow-cell and plugged into the Arduino-compatible reader board for transfer curve acquisition, c. The graphene FET chip layout with nine graphene channels that shows the position of the source (S), drain (D) and gate (G), and d. The optical micrograph shows a graphene channel's position flanking between gold contacts inside the chip.

2.2.2 Surface functionalization and DNA hybridization on the graphene FET chip

The graphene FET was gradually functionalized to obtain an effective detection signal before applying the microfluidic system, as shown in Figure 2a. First, the gold layer around the graphene channel was passivated overnight with 10 µL of 2 mM dodecanethiol (DDT) in an ethanol mixture. The graphene channel was treated with 10 µL of 10 mM of PBSE in dimethylformamide (DMF) for 2 hours. This non-covalent coupling was achieved through π-π stacking interactions between complementary aromatic rings in the graphene and the pyrene functional groups of PBSE, as reported in our previous studies [23], [31]. After washing with DMF, the chip was integrated into a complete assembly with the PDMS flow cell and microfluidic system, then rinsed by flowing 0.01x PBS for 30 min and a flow rate of 10 µL/s. Next, the probe molecules were introduced into the channel by injecting a 1 µM amine-tagged pDNA in 1× PBS and prolonged overnight to achieve saturation.

The effective immobilization of pDNA was done through the forward-reverse flow with a 20 s waiting time before flow inversions and a flow rate of 2 µL/s. After every 90 cycles of this process, a new pDNA solution was introduced. The pDNA was covalently grafted to the surface-bound PBSE molecules via amide bond formation with the amine group attached to the 3' end of the pDNA sequence. The functionalization process was continued with a 0.01x PBS washing through the channel for 30 min with a flow rate of 10 µL/s, followed by the10 mM ethanolamine (ETA) solution injection into the channel for 30 min with a flow rate of 10 µL/s to minimize the non-specific binding. In the last stage, after 30 min of 0.01x PBS rinsing, the

complementary or non-complementary tDNA solution with increasing concentration was injected into the channel via a forward-reverse flow described earlier at a flow rate of 2 µL/s for 30 min and waiting time of 20 s. Each sample exposure was followed by a washing step with 0.01× PBS buffer for another 30 min for sensor regeneration, and the represented signal was extracted from the last 10 Dirac point values of the measurement in the buffer. The signal acquisition optimization is studied through drifts transition in the integrated device depicted in the Supplementary Materials (Figure S3). The washing step was constantly done by injecting the buffer from a specific buffer reservoir using the syringe pump, while the multi-port valves were used for selecting and controlling the sample injection. The overall sequential microfluidic task execution commands were loaded in the software interface and mostly run autonomously throughout the experiment.

Each surface functionalization stage from DDT passivation of the gold layer, coupling of PBSE to graphene, binding pDNA to PBSE, ETA blocking, and finally, the tDNA hybridization with pDNA was confirmed by Raman spectroscopy and Dirac point analyses recorded with the portable platform. The details of the graphene surface modification in the FET chip before using it as sensors follow our previously reported work [23] and are depicted in Figure 2a. Whereas, Figure 2b illustrates the mechanism of the Dirac voltage shift (ΔV_{Dirac}) before and after the DNA hybridization event on the graphene FET sensor.

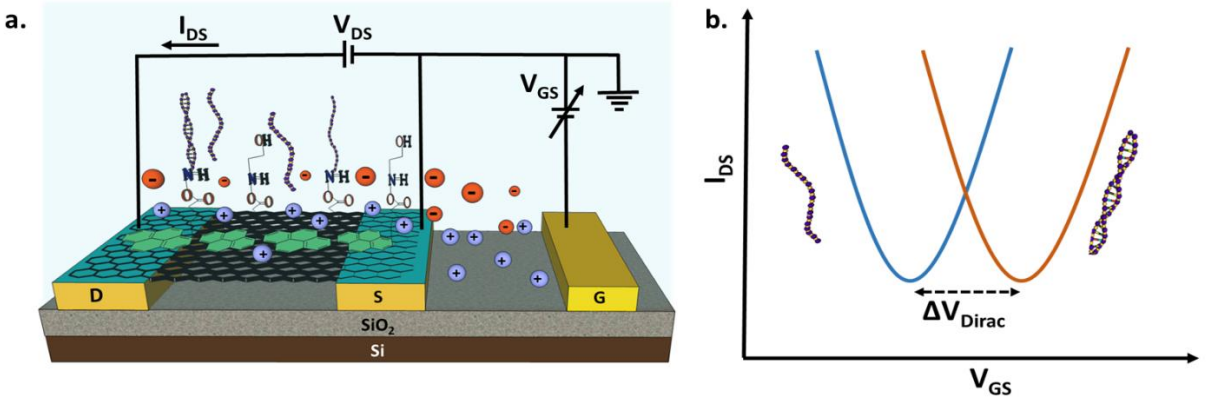

Figure 2. a. Graphene FET sensor surface functionalization and the setup with drain (D), source (S), and gate (G) electrodes, and b. DNA hybridization sensing principles according to interfacial charge-induced Dirac voltage shift (ΔV_{Dirac}) in the graphene FET sensor

2.2.3 Electrical characterization

The measurement of the Dirac point of the graphene FET chip was performed by plugging the chip into an Arduino-compatible custom board with the size of 10×6 cm^2 equipped with a microcontroller, digital-to-analog, and analog-to-digital (DAC, ADC) converters, resistance-controlled current source of 1-100 µA, digital potentiometer and CMOS matrices. A constant drain-source current (I_{DS}) was applied at 1.5 µA. The liquid gate voltage was linearly scanned from 0.2 to 1.2 V with a voltage step of 7.5 mV using a liquid gate electrode. One measurement consists in measuring the 9 sensors successively with 1s waiting time between each measurement of the transfer curve. For all the electrical measurements after the PBSE functionalization stage, a continuous mode of transfer curve recording was applied for the kinetic study of pDNA immobilization and transient real-time monitoring of DNA hybridization.

3. Results and Discussion

A graphene quality assessment was performed before using the graphene FET chip for the DNA sensor. Figure 3a shows the optical microscope photograph of the CVD-grown graphene layer after the transfer process onto SiO_2/Si substrate, resulting in relatively homogenous coverage with small graphene crystallites appearance and a minimal trace of PMMA. In Figure 3b, Raman spectroscopy analysis further revealed the near fully monolayer graphene with relatively low defects seen in the 2D (~2696 cm^{-1})/G (~1594 cm^{-1}) intensity ratio (I_{2D}/I_G) of around 1.30, without the appearance of a D peak (~1351 cm^{-1}). The passivation of the Au contact area with thiols by the DDT leaves the monolayer graphene functionality intact, as seen in the behavior of the comparatively similar Raman peaks to the bare graphene. Minor defects on the graphene post-PBSE treatment occurred, indicated by the existence of the D peak at ~1349 cm^{-1} as the impact of the p-orbital hybridization of PBSE molecule with graphene in-plane electrons. We also observed D' peak's appearance at ~1623 cm^{-1} adjacent to the G peak after PBSE treatment, implying additional impurities and charges on top of the graphene. The presence of D and D' peaks is attributed to the relative resonance of sp3 bonding and a pyrene group in the binding of PBSE to the graphene surface [31], [32]. A slight left shift of the 2D and G peaks to ~2679 and ~2594 cm^{-1}, respectively, was due to the doping effect from the presence of N in the DMF solvent molecule. In addition, the slight change in the I_{2D}/I_G ratio after PBSE functionalization indicates that PBSE contributes to doping effects on graphene by the presence of the carbonyl group (electron acceptor) in PBSE [33]. In Figure 3c, 2D confocal Raman spectroscopy mapping performed over a scanning area of ~90 μm^2 reveal that the I_{2D}/I_G ratio falls in the range of 1.3-1.8, indicating the monolayer character of graphene. We also observed a few locations on the graphene with $I_{2D}/I_G<1$ due to new seed development underneath the monolayer graphene that did not progress to form a bilayer.

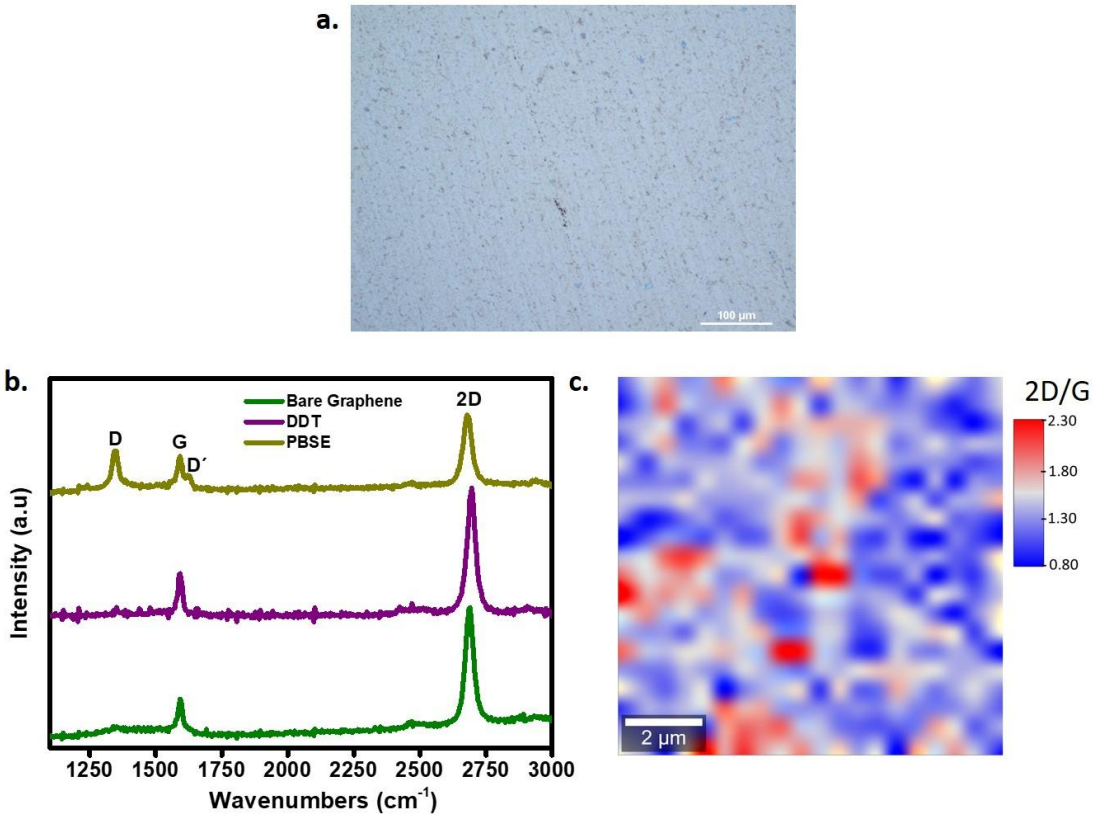

Figure 3. a. Optical micrograph of as-transferred monolayer graphene onto SiO_2/Si substrate, b. Raman spectra with peak identifiers of bare graphene, after DDT passivation of the Au contacts, and after PBSE functionalization. The depicted spectra are averages of spectra taken

at several points over the samples, c. the corresponding 2D/G Raman intensity ratio (I_{2D}/I_G) maps of the monolayer graphene.

The transfer curves characteristic of graphene after step-by-step surface modification are shown in Figure 4a. The DDT passivation on Au contacts and the attachment of PBSE onto the graphene channel were done outside the microfluidic system to avoid damage due to prolonged exposure to the DMF (the PBSE diluent). The real-time measurement incorporating the automated microfluidic system is started by measuring the signal after PBSE functionalization, followed by the rest of the DNA probing and hybridization process. ΔV_{Dirac} is positive or negative depending on the type and concentration of the charged species. The doping effect by charge transfer is dominant at a low concentration of the adsorbed species. On the contrary, local gating effects occur at a high concentration of adsorbed charged species where the distance between the adsorbed species is comparable to or smaller than the Debye length [34]. Au passivation by DDT is crucial to prevent DNA adsorption onto the gold, disrupting the measurement. Figure 4a shows that the "V"-shaped transfer curve shifts to lower voltage after DDT treatment. The dense self-assembled monolayer (SAM) of DDT on the Au contact changes the composition of the gate surface [24]. The DDT contributes to net positive charges on the Au surface, which increases the electric field when the gate voltage is applied. This effect results in gating enhancement and Dirac point shifting toward lower voltages [31]. Next, consistent with several reported works [35], [36], π-π stacking due to PBSE attachment intensifies the p-doping effect on graphene, shifting the voltage positively. Immobilizing the highly charged pDNA molecule on graphene results in a positive ΔV_{Dirac}, interpreted as the electrical double layer (EDL)-mediated capacitive coupling between the negatively charged nucleotide phosphate backbones and the graphene. To block the non-specific binding onto the NHS-ester ligands of PBSE, ETA is injected onto the sensing area and generates a negative ΔV_{Dirac} due to eliminating the non-bonded and weakly bonded pDNA and consequent removal of negative charge. The probe DNA crosslinking on the PBSE linker and the hybridization are characterized in Raman spectra shown in Figure S3 and Table S1 in the Supplementary Materials.

Figure 4b presents the continuous real-time measurement of the probe DNA immobilization onto the graphene FET chip using the programmable microfluidic system. We used impinging jet flow geometry over the embedded sensor, where the inlet and outlet of the PDMS flow cell are located side by side [37], instead of putting them in a straight line (channel flow type) position (Figure S2). It aims to achieve more even spreading liquid onto the entire sensing surface area since the fluid will only pass the outlet if the well is full, spontaneously generating pressure to outflow. The gasket lies under the channel holes; it helps seal the cell and prevents fluid leakage. The PMMA solid support clamps the flow cell in a fixed position and controls the pressure imposed on the sensing surface during the liquid injection. After washing with PBS, the infusion of pDNA through the flow cell into the sensing area gradually increases the Dirac voltage, stabilizing after about 180 min. We prolonged this procedure overnight to mimic the procedure of pDNA immobilization typically performed in static drop mode, and the signal was considerably steady. The mixing of pDNA solution through reverse and forward flow (mixing) with a constant flow rate of fluid aspiration and dispensing fosters the kinetic activity of the pDNA and accelerate the immobilization efficiency. A low flow rate for this mixing procedure (2 µL/s) was preferred to provide fluidics coupling onto the sensor; this minimized the pressure change and the local concentration gradient, which is likely to happen every time new batches of pDNA solution diffuse onto the sensing surface. A low flow rate also provides reaction rate stability, particularly for a long-run measurement, and keeps pDNA solution consumption to a low volume. After the pDNA immobilization step, ETA was injected and

flowed for 30 min. The reduction of Dirac voltage in real-time is depicted (Figure 4b) in this period, indicating the successful removal of non-specific molecular binding onto the modified graphene FET.

Theoretically, every resulting kinetic model representing adsorption kinetics at solid/liquid interfaces provides a unique adsorption curve property [38]. This section compares the resulting time-dependent ssDNA surface coverage (Γ) with the Langmuir and Freundlich models. The parameters of these models were calculated by the non-linear regression method using Origin 9.0 software (OriginLab Corporation, MA, USA). The Langmuir isotherm assumes the single-layer coverage of the adsorbed species over a homogeneous adsorbent surface where only similar sites are available for adsorption with equal adsorption energies. Thus, once a DNA molecule is immobilized at a specific site, no further adsorption can occur at the site. The most straightforward Langmuir equation is as follows [39]:

$$\frac{d\Gamma(t)}{dt} = k_a C_0 \left(1 - \frac{\Gamma(t)}{\Gamma max}\right) \qquad (1)$$

where k_a is the adsorption constant, C_0 is the ssDNA initial concentration, and Γmax is the maximum surface coverage. Furthermore, the contribution to the voltage signal from free ssDNA in solution on our graphene FET interface could be negligible. Considering that the voltage signal (V) is proportional to the surface coverage Γ, equation (1) can be modified into:

$$\frac{V(t)}{V_{max}} = 1 - e^{\frac{-k_a C_0 t}{V_{max}}} \qquad (2)$$

where V_{max} is the maximum voltage signal when the pDNA probe immobilization reaches saturation. As a comparison, the real-time pDNA signal was also fitted to the Freundlich adsorption isotherm. This model assumes that the adsorbent consists of a heterogeneous surface composed of different classes of adsorption sites which possibly result in multilayer adsorption with a represented equation as follows:

$$V_{(t)} = K_f \, {C_0}^{1/n} \qquad (3)$$

where K_f is a constant of the adsorption capacity of the adsorbent, and n is the Freundlich coefficient [40]. Model fitting to equilibrium adsorption results of DNA was assessed based on the correlation coefficient (R^2) values, reflecting the relationship between the adsorption data and the theoretical models. As shown in Figure 4c, the R^2 value for the Langmuir isotherm was higher (R^2 = 0.981) than that of the Freundlich isotherm (R^2 = 0.945) for the adsorption of pDNA onto the modified graphene FET surface. These results suggest that single-stranded pDNA immobilization onto the graphene FET surface through chemical bonding with PBSE linker follows the monolayer adsorption mechanism.

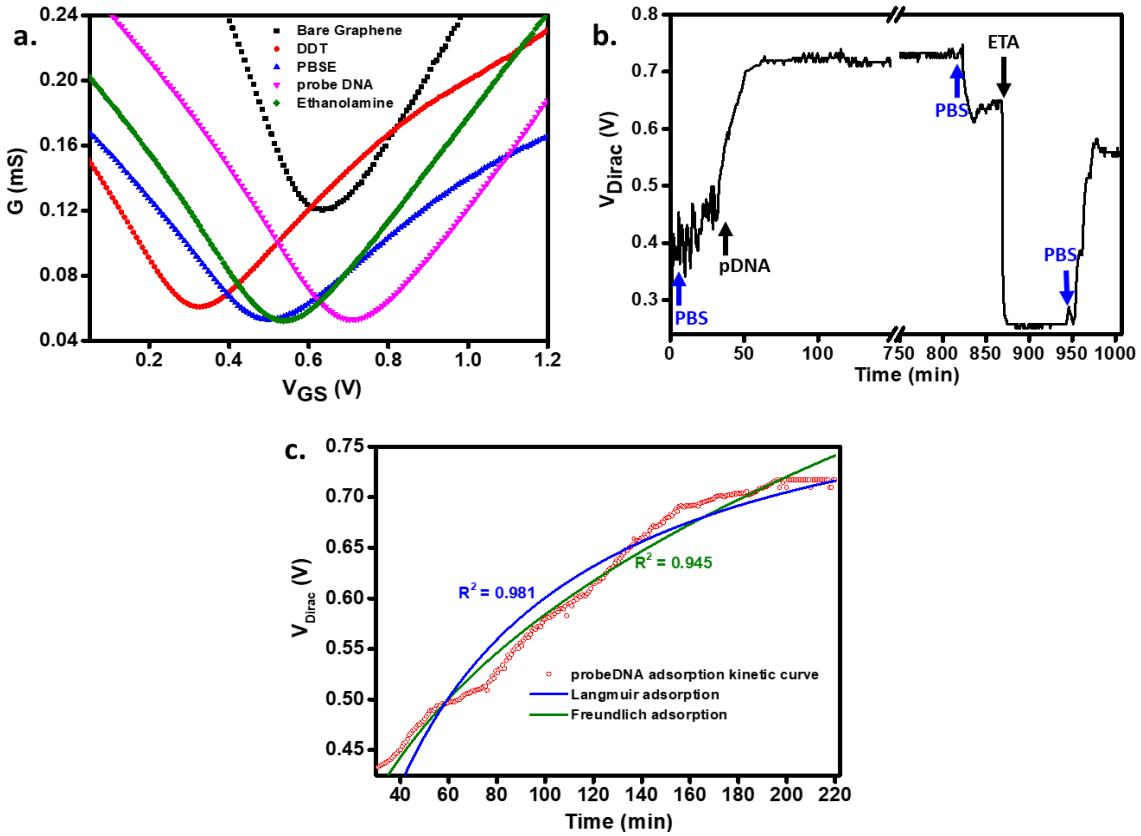

Figure 4.a. Transfer curve characteristics of step-by-step surface modification on graphene FET sensor, b. The continuous real-time screening of the pDNA immobilization and ETA blocking on graphene FET sensor using programmable microfluidic device showing a stable response over long-run measurement, c. Adsorption kinetic curves of the pDNA immobilization on the modified graphene FET sensor fitted with Langmuir and Freundlich isotherm models.

Real-time DNA hybridization screening was performed in 30 min, by a list of programmed commands in the microfluidic software to perform a series of autonomous tasks similarly used in the pDNA immobilization. Figure 5a and b display the time-dependent data points of DNA hybridization in the microfluidic setup for complementary and non-complementary tDNA, respectively. The red arrows indicate when the tDNA containing vial valve releases the solution onto the flow cell, in a concentration range between 1 aM and 10 pM. After tDNA injection, the Dirac voltage signal exponentially increases until it reaches a steady-state as typically reported in microfluidic-based sensors [18], [41], [42]. This stage lasts for 30 minutes. Subsequently, a PBS wash is run into the flow cell to dissociate and remove the target from the weak hybridization sites (see Figure 5c). The V_{Dirac} measurement for each concentration is taken another 30 minutes after the PBS washing step starts (a yellow solid star sign indicates this moment in Figure 5). This delay ensures that the signal results from the fully hybridized probe-target pairs at each tDNA concentration. The ΔV_{Dirac} is obtained by subtracting the baseline (blank signal) from V_{Dirac} after hybridization. The sharp spikes around the introduction times of the target analytes and the PBS buffer are noise associated with automated valving changes from DNA to PBS channels and the impact of the flow cell interfacial pressure change and transient concentration gradients. Figure 5a shows that larger Dirac voltage shifts occur in the hybridization events of the pDNA and complementary tDNA than corresponding V_{Dirac} shifts for the non-complementary tDNA (Figure 5b). Moreover, in the complementary DNA hybridization measurement, after the tDNA injection, the signal stabilization took longer (~20 min) than in the non-complementary hybridization (~10 min). This longer time could result

from more matching strands in the entirely complementary sequence, requiring longer period to align and bind with every vacant probe strand. In contrast, in the non-complementary hybridization, a faster steady point is reached since the Dirac point is mainly produced by random nucleobase affinity and not by full strand hybridization events and is thus easily washed away by the buffer. It is also noted, particularly in the complementary DNA hybridization (Figure 5a), that the noise in the baseline signal (in the PBS wash between hybridization periods) is more visible at low tDNA concentrations (1 and 10 aM) followed by the behavior of slow, gradual increment with more steady baseline signals at higher concentrations (100 aM-10 pM). These effects occur since, for very low tDNA concentration, the PBS washing step is faster than for higher concentrations. In the latter case, the non- or weakly bonded tDNA removal is long enough to be captured and resolved in the measurement time frame.

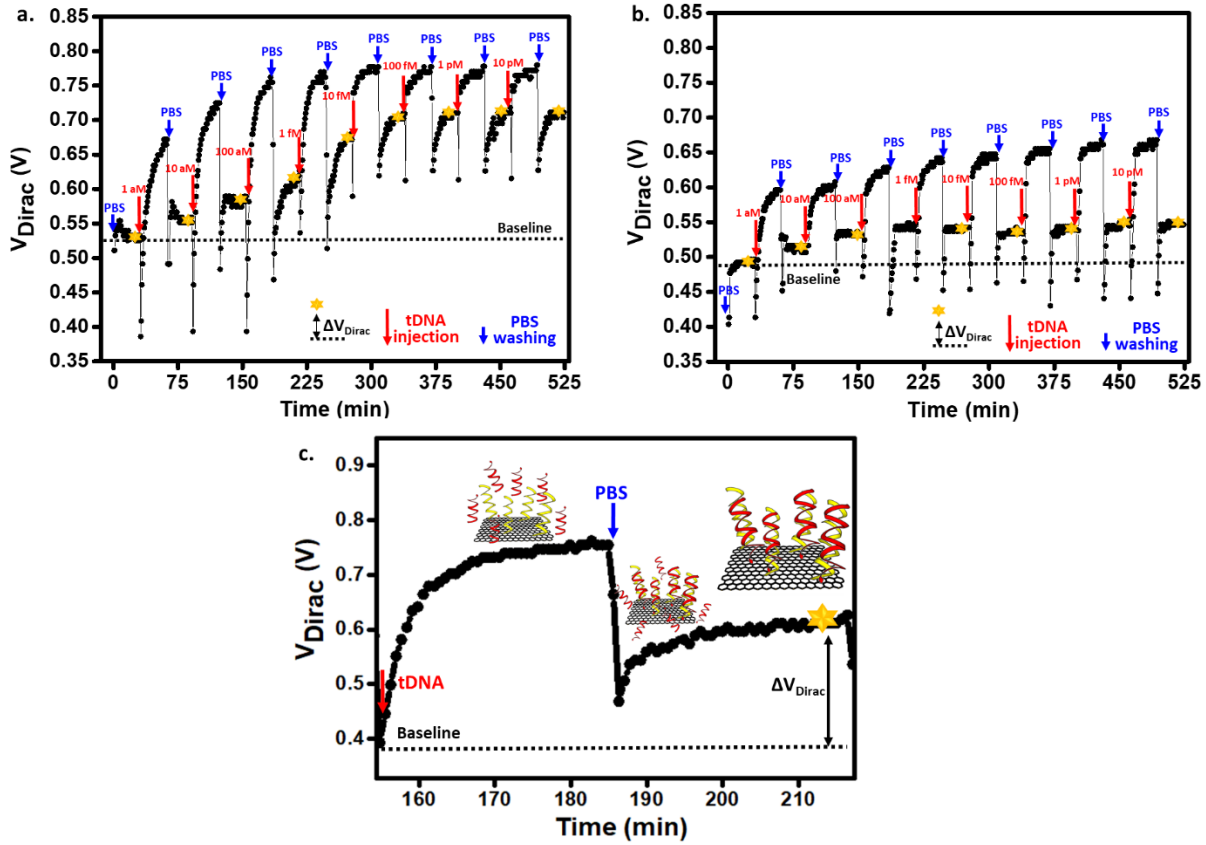

Figure 5. The continuous real-time screening of tDNA hybridization with pDNA in a series of concentrations of a. comp-tDNA and b. non-comp-tDNA using the programmable microfluidic system, c. schematic illustration of the processes occurring in the measuring time for a given tDNA concentration.

The transfer curves for both complementary and non-complementary DNA hybridization measurements on the graphene FET sensor are shown in Figure 6. Exposure to the lowest target DNA concentration (1 aM) for the complementary sequence resulted in a 26 mV Dirac voltage shift (ΔV_{Dirac}) in the positive direction with respect to V_{Dirac} of 0.522 V at a zero target DNA concentration (Figure 6a). The increasing concentration of comp-tDNA continuously shifted V_{Dirac} to a higher voltage until the saturation point was achieved at ~10 fM. This positive shift is caused by the accumulation of negative charge of DNA phosphate backbones in the vicinity to the transistor channel, increasing the electrostatic energy of electronic states in the graphene, which effectively moves the electrochemical potential towards the valence band, resulting in the p-doping of the graphene. Figure 6b shows the concentration-dependent calibration curve

obtained by plotting the ΔV_{Dirac} relative to the blank sample with a ~44 mV/decade tDNA concentration sensitivity. The characteristics of the non-linear response to increasing complementary target DNA concentration in the calibration plots fit well the modified Hill's function (Table S2) with an estimated limit of detection (LoD) of ~0.642 aM, making it one of the most sensitive detectors to date with outstanding versatility in the automated programmable microfluidic system integration in comparison with other reported works on biosensors (Table 2).

A similar shifting direction was obtained when the pDNA was hybridized with the non-comp-tDNA. However, as presented in Figure 6c, the ΔV_{Dirac} of 1 aM of the non-comp-tDNA sequence showed a lower value (20 mV) with respect to the V_{Dirac} of 0.476 V of the blank sample. This attenuated sensor response indicates that the non-complementary sequence also possesses affinity toward the non-matching pDNA by random and natural single-nucleotide pairing behavior, although with weaker binding than the complete set of complementary base pairs. Subsequently, with a higher concentration of the non-complementary sequence, the hybridization event still shifted the Dirac voltage to the right, but showed a more rapid saturation point, reached at a non-comp-tDNA concentration of 100 aM. Figure 6d depicts the calibration plots for non-comp-tDNA hybridization with a sensitivity as low as ~14 mV/decade. These results suggest the high specificity of the surface modification model of the graphene FET sensor and the integrated microfluidic system.

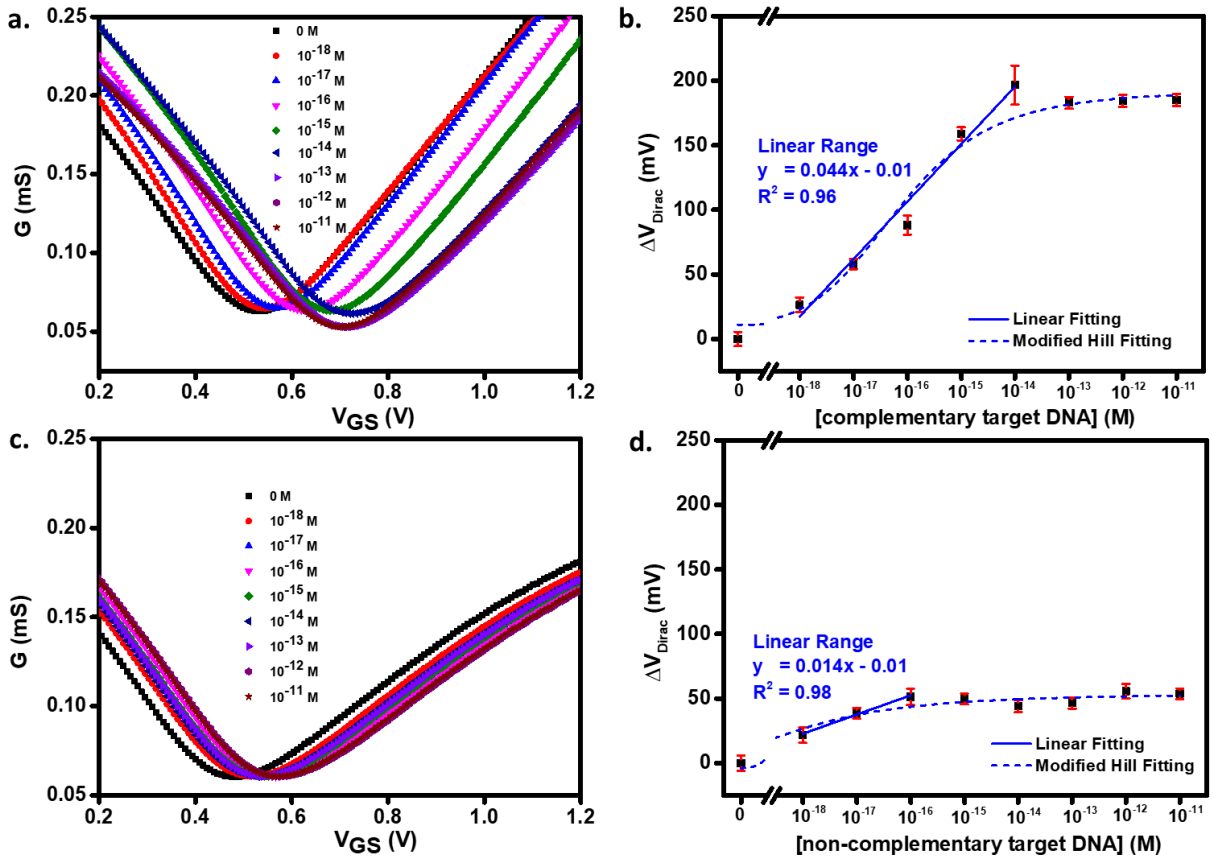

Figure 6a. Transfer curves characteristics of graphene FET and b. Concentration-dependent calibration curves of DNA hybridization detection using complementary target sequence, and c. Transfer curves characteristics of graphene FET and d. Concentration-dependent calibration curves of DNA hybridization detection using non-complementary target sequence.

Table 2. The performance comparison of the current work with previously published research in various biosensor setups.

Sensors	MF integration	Automated/ Programmable MF	Target Analyte	Dynamic range	Sensitivity	LoD	Ref
Printed graphene FET	No	No	DNA	100 pM-1 uM	30.1 mV/dec	1 nM	[43]
Fluorescence quenching on gold	Yes	No	Streptavidin (DNA assisted)	1 pM-10 nM	n.a	60 aM	[44]
AuNPs decorated Graphene FET	Yes	No	Bisphenol A (DNA assisted)	10^{-5} – 10^{4} ng/mL	n.a	10 ng/mL	[45]
Graphene FET	Yes	No	Thrombin	0 pM – 1 uM	n.a	2.6 pM	[46]
Graphene FET	Yes	No	Exosome	0.1-10 ug/mL	n.a	n.a	[28]
Poly-L-Lysine (PLL) substrate	Yes	No	miRNA	10^{-12} - 10^{-7}M	n.a	1 pM	[47]
MoS_2/Carbon Nanotube Nanocomposites	Yes	No	DNA	0-200 nM	n.a	1 nM	[48]
Gold LSPR Substrate	Yes	No	DNA polymerase	n.a	n.a	0.0625 U/mL polymerase	[49]
Graphene FET	Yes	Yes	DNA	1 aM – 10 pM	~44 mV/dec	~0.6 aM	This work

Conclusion

Developing a lab-on-a-chip (LoC) system with full automation is increasingly required in many applications. This study developed an integrated microfluidic system with a graphene FET sensor for DNA detection. The assembled device enables real-time biochemical reaction screening onto the sensing surface by dual built-in digital controls from a portable graphene curve reader and microfluidic software. The graphene FET chip constructed with modified monolayer graphene showed excellent interfacial coupling properties for oligonucleotide adsorption and hybridization. The delivery of fluids on the graphene FET chip performed with programmable flowthrough addressable multi-position valves shows important features in executing synchronous/asynchronous sequential and parallel bioanalysis autonomously. The proposed prototype offers multiple advantages, including high sensitivity, minimal user intervention, and a miniaturized setting. This technology holds promising potential to detect various target analytes and incorporate data transmission for remote and decentralized analysis and monitoring.

Acknowledgment

This research is supported by PORTGRAPHE-Control of Port and Douro Wines authenticity using graphene DNA sensors project co-funded by FCT (PTDC/BIA-MOL/31069/2017) and the ERDF through COMPETE2020 (POCI-01-0145-FEDER-031069). One of the authors (T.D.) acknowledges a Ph.D. grant from FCT (SFRH/BD/08181/2020). FCT partially supported UMinho's research in the Strategic Funding UIDB/04650/2020.

References

[1] D. E. W. Patabadige, S. Jia, J. Sibbitts, J. Sadeghi, K. Sellens, and C. T. Culbertson, "Micro Total Analysis Systems: Fundamental Advances and Applications," *Anal. Chem.*, vol. 88, no. 1, pp. 320–338, 2016.

[2] J. Zhuang, J. Yin, S. Lv, B. Wang, and Y. Mu, "Advanced' lab-on-a-chip' to detect viruses – Current challenges and future perspectives," *Biosens. Bioelectron.*, vol. 163, p. 112291, 2020.
[3] C. Tymm, J. Zhou, A. Tadimety, A. Burklund, and J. X. J. Zhang, "Scalable COVID-19 Detection Enabled by Lab-on-Chip Biosensors," *Cell. Mol. Bioeng.*, vol. 13, no. 4, pp. 313–329, 2020.
[4] M. K. Kansiime, J. A. Tambo, I. Mugambi, M. Bundi, A. Kara, and C. Owuor, "COVID-19 implications on household income and food security in Kenya and Uganda: Findings from a rapid assessment," *World Dev.*, vol. 137, p. 105199, 2021.
[5] N. S. Diffenbaugh *et al.*, "The COVID-19 lockdowns: a window into the Earth System," *Nat. Rev. Earth Environ.*, vol. 1, no. 9, pp. pages470–481, 2020.
[6] J. Gaughran, D. Boyle, J. Murphy, R. Kelly, and J. Ducrée, "Phase-selective graphene oxide membranes for advanced microfluidic flow control," *Microsystems Nanoeng.*, vol. 2, no. 1, p. 16008, 2016.
[7] C. Watson and S. Senyo, "All-in-one automated microfluidics control system," *HardwareX*, vol. 5, p. e00063, 2019.
[8] A. Atay *et al.*, "Flow rate-controlled pipetting for microfluidics: second-generation flexible hydraulic reservoir (FHRv2)," *Microfluid. Nanofluidics*, vol. 25, no. 1, p. 3, 2021.
[9] A. Ozcelik and Z. Aslan, "A practical microfluidic pump enabled by acoustofluidics and 3D printing," *Microfluid. Nanofluidics*, vol. 25, no. 1, p. 5, 2021.
[10] K. S. Novoselov *et al.*, "Electric Field Effect in Atomically Thin Carbon Films Supplementary," *Science (80-.).*, vol. 306, no. 5696, pp. 666–669, 2004.
[11] S. Wu, X. Wang, Z. Li, S. Zhang, and F. Xing, "Recent advances in the fabrication and application of graphene microfluidic sensors," *Micromachines*, vol. 11, no. 12, p. 1059, 2020.
[12] S. B. Singh and C. M. Hussain, "Nano-Graphene as Groundbreaking Miracle Material: Catalytic and Commercial Perspectives," *ChemistrySelect*, vol. 3, no. 33, pp. 9533–9544, 2018.
[13] C. L. P. Pavithra, B. V. Sarada, K. V. Rajulapati, T. N. Rao, and G. Sundararajan, "A new electrochemical approach for the synthesis of copper-graphene nanocomposite foils with high hardness," *Sci. Rep.*, vol. 4, p. 4049, 2014.
[14] J. Keyte, K. Pancholi, and J. Njuguna, "Recent Developments in Graphene Oxide/Epoxy Carbon Fiber-Reinforced Composites," *Front. Mater.*, vol. 6, p. 224, 2019.
[15] E. Vermisoglou *et al.*, "Human virus detection with graphene-based materials," *Biosens. Bioelectron.*, vol. 166, p. 112436, 2020.
[16] S. K. Krishnan, E. Singh, P. Singh, M. Meyyappan, and H. S. Nalwa, "A review on graphene-based nanocomposites for electrochemical and fluorescent biosensors," *RSC Adv.*, vol. 9, no. 16, pp. 8778–8881, 2019.
[17] R. Z. A. Raja Jamaluddin, L. L. Tan, K. F. Chong, and L. Y. Heng, "An electrochemical DNA biosensor fabricated from graphene decorated with graphitic nanospheres," *Nanotechnology*, vol. 31, no. 48, p. 485501, 2020.
[18] B. A. Prabowo, A. Purwidyantri, B. Liu, H. C. Lai, and K. C. Liu, "Gold nanoparticle-assisted plasmonic enhancement for DNA detection on a graphene-based portable surface plasmon resonance sensor," *Nanotechnology*, vol. 32, no. 9, p. 095503, 2021.
[19] N. Singh *et al.*, "Dual-modality microfluidic biosensor based on nanoengineered mesoporous graphene hydrogels," *Lab Chip*, vol. 20, no. 4, pp. 760–777, Feb. 2020.
[20] S. Islam *et al.*, "Microfluidic-based graphene field effect transistor for femtomolar detection of chlorpyrifos," *Sci. Rep.*, vol. 9, no. 1, p. 276, 2019.

[21] Y. T. Kang *et al.*, "On-Chip Biogenesis of Circulating NK Cell-Derived Exosomes in Non-Small Cell Lung Cancer Exhibits Antitumoral Activity," *Adv. Sci.*, vol. 8, no. 6, p. 2003747, 2021.
[22] Y. Xia *et al.*, "Plasma treated graphene FET sensor for the DNA hybridization detection," *Talanta*, vol. 223, no. 2, p. 121766, 2021.
[23] A. Purwidyantri *et al.*, "Influence of the Electrolyte Salt Concentration on DNA Detection with Graphene Transistors," *Biosensors*, vol. 11, no. 1, p. 24, 2021.
[24] A. Purwidyantri *et al.*, "Sensing performance of fibronectin-functionalized Au-EGFET on the detection of S. epidermidis biofilm and 16S rRNA of infection-related bacteria in peritoneal dialysis," *Sensors Actuators B Chem.*, vol. 217, pp. 92–99, 2015.
[25] I. A. Vacchi, C. Ménard-Moyon, and A. Bianco, "Chemical Functionalization of Graphene Family Members," *Phys. Sci. Rev.*, vol. 2, no. 1, p. 20160103, 2017.
[26] V. Georgakilas *et al.*, "Noncovalent Functionalization of Graphene and Graphene Oxide for Energy Materials, Biosensing, Catalytic, and Biomedical Applications," *Chem. Rev.*, vol. 116, no. 9, pp. 5464–5519, 2016.
[27] C. Chan, J. Shi, Y. Fan, and M. Yang, "A microfluidic flowthrough chip integrated with reduced graphene oxide transistor for influenza virus gene detection," *Sensors Actuators, B Chem.*, vol. 251, pp. 927–933, 2017.
[28] D. Kwong Hong Tsang *et al.*, "Chemically Functionalised Graphene FET Biosensor for the Label-free Sensing of Exosomes," *Sci. Rep.*, vol. 9, no. 1, pp. 2–11, 2019.
[29] M. T. Hwang *et al.*, "Ultrasensitive detection of nucleic acids using deformed graphene channel field effect biosensors," *Nat. Commun.*, no. 11, p. 1543, 2020.
[30] N. Gao *et al.*, "Specific detection of biomolecules in physiological solutions using graphene transistor biosensors," *Proc. Natl. Acad. Sci. U. S. A.*, vol. 113, no. 51, 2016.
[31] R. Campos *et al.*, "Attomolar label-free detection of dna hybridization with electrolyte-gated graphene field-effect transistors," *ACS Sensors*, vol. 4, no. 2, pp. 286–293, 2019.
[32] G. Seo *et al.*, "Rapid Detection of COVID-19 Causative Virus (SARS-CoV-2) in Human Nasopharyngeal Swab Specimens Using Field-Effect Transistor-Based Biosensor," *ACS Nano*, vol. 14, no. 4, pp. 5135–5142, 2020.
[33] G. Wu, X. Tang, M. Meyyappan, and K. W. C. Lai, "Doping effects of surface functionalization on graphene with aromatic molecule and organic solvents," *Appl. Surf. Sci.*, vol. 425, pp. 713–721, 2017.
[34] S. Mao *et al.*, "Two-dimensional nanomaterial-based field-effect transistors for chemical and biological sensing," *Chem. Soc. Rev.*, vol. 46, no. 22, pp. 6872–6904, 2017.
[35] W. Yue *et al.*, "An electricity-fluorescence double-checking biosensor based on graphene for detection of binding kinetics of DNA hybridization," *RSC Adv.*, vol. 7, no. 70, pp. 44559–44567, 2017.
[36] N. M. Andoy, M. S. Filipiak, D. Vetter, Ó. Gutiérrez-Sanz, and A. Tarasov, "Graphene-Based Electronic Immunosensor with Femtomolar Detection Limit in Whole Serum," *Adv. Mater. Technol.*, vol. 3, no. 12, p. 1800186, 2018.
[37] D. J. Pike, N. Kapur, P. A. Millner, and D. I. Stewart, "Flow cell design for effective biosensing," *Sensors (Switzerland)*, vol. 13, no. 1, pp. 58–70, 2013.
[38] A. W. Peterson, R. J. Heaton, and R. Georgiadis, "Kinetic control of hybridization in surface immobilized DNA monolayer films," *J. Am. Chem. Soc.*, vol. 122, no. 32, pp. 7837–7838, 2000.
[39] J. Wu, H. Wang, A. Zhu, and F. Long, "Adsorption Kinetics of Single-Stranded DNA on Functional Silica Surfaces and Its Influence Factors: An Evanescent-Wave Biosensor Study," *ACS Omega*, vol. 3, no. 5, pp. 5605–5614, 2018.
[40] N. Chaouati, A. Soualah, and M. Chater, "Adsorption of phenol from aqueous solution

onto zeolites y modified by silylation," *Comptes Rendus Chim.*, vol. 16, no. 3, pp. 222–228, 2013.
[41] A. Poghossian, M. Jablonski, D. Molinnus, C. Wege, and M. J. Schöning, "Field-Effect Sensors for Virus Detection: From Ebola to SARS-CoV-2 and Plant Viral Enhancers," *Front. Plant Sci.*, vol. 11, p. 598103, 2020.
[42] K. Asano *et al.*, "Real-Time Detection of Glyphosate by a Water-Gated Organic Field-Effect Transistor with a Microfluidic Chamber," *Langmuir*, vol. 37, no. 24, pp. 7305–7311, 2021.
[43] S. Papamatthaiou, P. Estrela, and D. Moschou, "Printable graphene BioFETs for DNA quantification in Lab-on-PCB microsystems," *Sci. Rep.*, vol. 11, no. 1, p. 9815, 2021.
[44] J. Wang *et al.*, "Microfluidic biosensor for the detection of DNA by fluorescence enhancement and the following streptavidin detection by fluorescence quenching," *Biosens. Bioelectron.*, vol. 51, pp. 280–285, 2014.
[45] S. Liu, Y. Fu, C. Xiong, Z. Liu, L. Zheng, and F. Yan, "Detection of Bisphenol A Using DNA-Functionalized Graphene Field Effect Transistors Integrated in Microfluidic Systems," *ACS Appl. Mater. Interfaces*, vol. 10, no. 28, pp. 23522–23528, 2018.
[46] N. I. Khan, M. Mousazadehkasin, S. Ghosh, J. G. Tsavalas, and E. Song, "An integrated microfluidic platform for selective and real-time detection of thrombin biomarkers using a graphene FET," *Analyst*, vol. 145, no. 13, pp. 4494–4503, 2020.
[47] Y. Gao, L. Qiang, Y. Chu, Y. Han, Y. Zhang, and L. Han, "Microfluidic chip for multiple detection of miRNA biomarkers in breast cancer based on three-segment hybridization," *AIP Adv.*, vol. 10, no. 4, p. 045022, 2020.
[48] D. Yang, M. Tayebi, Y. Huang, H. Y. Yang, and Y. Ai, "A microfluidic DNA sensor based on three-dimensional (3D) hierarchical MoS2/carbon nanotube nanocomposites," *Sensors (Switzerland)*, vol. 16, no. 11, p. 1911, 2016.
[49] J. Roether, K. Y. Chu, N. Willenbacher, A. Q. Shen, and N. Bhalla, "Real-time monitoring of DNA immobilization and detection of DNA polymerase activity by a microfluidic nanoplasmonic platform," *Biosens. Bioelectron.*, vol. 142, p. 111528, 2019.